

A study of the H I gas fractions of galaxies at $z \sim 1$

Wei Zhang¹, Guinevere Kauffmann², Jing Wang³, Yanmei Chen^{4,5}, Jian Fu^{6,7}, Hong Wu¹

¹ CAS Key Laboratory of Optical Astronomy, National Astronomical Observatories, Chinese Academy of Sciences, Beijing 100101, China

e-mail: xtwfn@bao.ac.cn

² Max Planck Institut für Astrophysik, Karl-Schwarzschild-Strasse 1, 85748 Garching, Germany

³ Kavli Institute for Astronomy and Astrophysics, Peking University, Beijing 100871, China

⁴ School of Astronomy and Space Science, Nanjing University, Nanjing 210093, China

⁵ Key Laboratory of Modern Astronomy and Astrophysics (Nanjing University), Ministry of Education, Nanjing 210093, China

⁶ Shanghai Astronomical Observatory, 80 Nandan Road, Shanghai 200030, China

⁷ Key Laboratory for Research in Galaxies and Cosmology, Shanghai Astronomical Observatory, CAS, 80 Nandan Road, Shanghai 200030, China

Received; accepted

ABSTRACT

Aims. Due to the fact that H I mass measurements are not available for large galaxy samples at high redshifts, we apply a photometric estimator of the H I-to-stellar mass ratio (M_{HI}/M_*) calibrated using a local Universe sample of galaxies to a sample of galaxies at $z \sim 1$ in the DEEP2 survey. We use these H I mass estimates to calculate H I mass functions (HIMFs) and cosmic H I mass densities (Ω_{HI}), and to examine the correlation between star formation rate and H I gas content, for galaxies at $z \sim 1$.

Methods. We have estimated H I gas masses for $\sim 7,000$ galaxies in the DEEP2 survey with redshifts in the range $0.75 < z < 1.4$ and stellar masses $M_* \gtrsim 10^{10} M_\odot$, using a combination of the rest-frame ultraviolet-optical colour ($NUV - r$) and stellar mass density (μ_*) as a way to estimate M_{HI}/M_* .

Results. It is found that the high mass end of high- z H I mass function (HIMF) is quite similar to that of the local HIMF. The lower limit of $\Omega_{\text{HI,limit}} = 2.1 \times 10^{-4} h_{70}^{-1}$, obtained by directly integrating the H I mass of galaxies with $M_* \gtrsim 10^{10} M_\odot$, confirms that massive star-forming galaxies do not dominate the neutral gas at $z \sim 1$. We study the evolution of the H I mass to stellar mass ratio from $z \sim 1$ to today and find a steeper relation between H I gas mass fraction and stellar mass at higher redshifts. Specifically, galaxies with $M_* = 10^{11} M_\odot$ at $z \sim 1$ are found to have 3–4 times higher neutral gas fractions than local galaxies, while the increase is as high as 4–12 times at $M_* = 10^{10} M_\odot$. The quantity M_{HI}/SFR exhibits very large scatter, and the scatter increases from a factor of 5–7 at $z = 0$ to factors close to a hundred at $z = 1$. This implies that there is no relation between H I gas and star formation in high redshift galaxies. The H I gas must be linked to cosmological gas accretion processes at high redshifts.

Key words. galaxies: evolution – galaxies: distances and redshifts – galaxies: ISM

1. introduction

Cold gas plays a crucial role in galaxy formation and evolution, yet our understanding of the cold gas content of galaxies has been hampered for many years by the lack of direct H I line measurements for galaxies at high redshifts. In the local Universe, much data on local galaxies exists from surveys such as the H I Parkes All Sky Survey (HIPASS; Meyer et al. 2004) and the Arecibo Legacy Fast ALFA (ALFALFA) survey (Giovanelli et al. 2005) of H I 21-cm emission of galaxies. It should be noted that these surveys are limited to nearby galaxies ($z \lesssim 0.06$), and are relatively shallow (H I-to-stellar mass ratio $M_{\text{HI}}/M_* \gtrsim 10\%$). The extended GALEX Arecibo SDSS Survey (xGASS; Catinella et al. 2018) was designed to observed galaxies to a fixed detection limit in the quantity M_{HI}/M_* in order to detect small amounts of residual gas in galaxies in transition between the star-forming main sequence (Noeske et al. 2007) (star-forming galaxies that define the relation between the star formation rate and stellar mass at a given redshift) and the population of massive early-type galaxies at the same redshift where star formation has largely ceased. This survey pushed the M_{HI}/M_* detection limit down to $\sim 1.5\%$ for a sample of 1179 galaxies with stellar masses $10^9 M_\odot < M_* < 10^{11.5} M_\odot$ and redshifts in

the range $0.01 < z < 0.05$. For redshifts beyond this range, observations of H I in emission are available only for a handful of galaxies out to $z < 0.25$ (Catinella et al. 2008). The current highest redshift of an individual galaxy with a direct H I emission detection at $z = 0.376$ is reported by Fernández et al. (2016) from a study with the COSMOS H I Large Extragalactic Survey.

At higher redshifts, observations of H I in emission from individual galaxies are lacking. There have been recent attempts to estimate the *average* atomic gas content in star-forming galaxies at $z \sim 0.24$ (Lah et al. 2007) and $z \sim 1.3$ (Kanekar et al. 2016) and in cluster galaxies at $z \sim 0.37$ (Lah et al. 2009), by co-adding the 21-cm emission signals of few hundred galaxies. Chowdhury et al. (2020) have applied the same method to a larger sample of 7,653 star-forming galaxies at $z = 0.74 - 1.45$. Pen et al. (2009) proposed that the cosmic structure traced by atomic gas could be probed by measuring the three-dimensional intensity map of the H I gas in the universe. In a series of test-case applications, Pen and collaborators measured the clustering signal of H I gas by cross-correlating H I data cubes with optical surveys of galaxies in both the local universe (Pen et al. 2009) and at $z \sim 0.7$ (Chang et al. 2010) and $z \sim 0.8$ (Masui et al. 2013).

For redshifts above $z \sim 1$, information about atomic gas can be obtained through observations of intervening damped Ly α (DLA) or Mg II absorption-line systems in the spectra of background quasars. Surveys of DLAs and Mg II provide an estimate of the total co-moving volume density of neutral and cool (10^4 – 10^5 K) gas in the Universe (Rao et al. 2006, 2017; Prochaska & Wolfe 2009; Noterdaeme et al. 2012; Crighton et al. 2015). Noterdaeme et al. (2012) concluded that Ω_{HI} evolves mildly over the redshift range $2.3 < z < 3.5$, while Zafar et al. (2013) showed that no evolution of Ω_{HI} is found over the redshift range $1.5 < z < 5.0$. A recent study by Neeleman et al. (2016) at $z \sim 0.6$ is consistent with a gradual decline from $z = 2$ to today. Sánchez-Ramírez et al. (2016) found that there is a small but statistically significant evolution in Ω_{HI} from $z \sim 0$ to $z \sim 5$. More recently Chowdhury et al. (2020) found that the relation between H I mass and absolute blue magnitude does not evolve between $z = 1$ and $z = 0$ (see also Walter et al. 2020).

We note that these results are in strong contrast to evolutionary studies of the CO luminosity function at high redshifts. The cosmic density of molecular gas in galaxies increases by a factor of 6 from the present day to $z \sim 1.5$ (Decarli et al. 2020). This is in qualitative agreement with the evolution of the cosmic star formation rate density over this redshift interval, suggesting that the molecular gas depletion time is approximately constant with redshift. The much weaker trend in Ω_{HI} with redshift would argue that the gas traced by H I is a transient phase, connected more intrinsically to ongoing gas accretion from the large-scale environment of the galaxy, rather than to star formation processes occurring in galactic disks or bulges.

Due to the fact that individual H I mass measurements are not available for large galaxy samples at high redshifts, there have been attempts to calibrate a variety of galaxy properties (usually UV or optical fluxes combined with stellar mass and other structural parameters) as proxies for the gas to stellar mass ratio. The H I gas-to-stellar mass ratio, M_{HI}/M_* , has been found to correlate well with, and so can be estimated from, the optical-optical (e.g. $u - r$) and optical-NIR (e.g. $u - K$) colours with a typical scatter of ~ 0.4 dex (Kannappan 2004, hereafter K04). (We note that, based on higher quality data, a scatter of ~ 0.3 dex has been found for an estimator of M_{HI}/M_* based only on colour by Eckert et al. (2015).) After that, some studies have focused on improving photometric estimators of M_{HI}/M_* by defining a gas-fraction ‘plane’ linking M_{HI}/M_* , stellar surface mass density, and optical (Zhang et al. 2009) or near-ultraviolet (NUV)-optical (Catinella et al. 2010) colour. The scatter in the H I mass fractions predicted by these estimators is typically ~ 0.3 dex in $\log M_{\text{HI}}/M_*$. In a more recent study, Li et al. (2012) further included Δ_{g-i} , the difference in $g - i$ colour between the outer and inner region of the galaxy, in order to generate accurate predictions for a population of massive galaxies with higher-than-average H I fractions, which were discovered by Wang et al. (2011) to have bluer, more actively star-forming outer discs. This estimator is demonstrated to provide unbiased M_{HI}/M_* estimates even for the most H I-rich galaxies in the ALFALFA survey. Such photometric estimators have been applied in a number of recent studies to determine whether the offset of a galaxy from the mean mass-metallicity relation depends on its gas content (Zhang et al. 2009), to study the dependence of galaxy clustering on H I mass fraction (Li et al. 2012), (Kauffmann et al. 2013), and to analyze the gas depletion of galaxies in clusters (Zhang et al. 2013). All these studies are limited to low-redshift galaxies in the SDSS with $z \lesssim 0.3$.

In this paper we extend this previous work by applying a photometric estimator of M_{HI}/M_* calibrated using a local Universe sample of galaxies to a sample of $\sim 7,000$ galaxies with $0.75 < z < 1.4$ in the DEEP2 survey (Davis et al. 2003). The estimator is based on the correlation between M_{HI}/M_* and rest-frame $NUV - r$ colour and galaxy size, and is calibrated using 660 local galaxies that have real H I emission line observations. This provides us with an H I mass estimate for each galaxy in our sample, thus allowing the H I mass function, the cosmic H I mass density and the correlation between atomic gas mass and galaxy properties such as stellar mass and star formation rate to be studied for the first time for a large set of galaxies at $z \sim 1$. We caution that the conclusions reached in our work rely on the assumption that the relation between H I mass fraction and $NUV - r$ colour and galaxy size in the local Universe applies at high redshifts.

The structure of our paper is as follows. In the following section, we describe the local galaxy sample used for calibrating our H I mass fraction estimator, as well as the DEEP2 galaxy sample. Our results are presented in §3, where we first present the H I-to-stellar mass estimator. We then apply the estimator to the DEEP2 galaxies to study the H I mass function (HIMF) (§3.2) and H I mass density Ω_{HI} (§3.3). Finally we investigate the correlations between gas fraction, stellar mass, specific star formation rate and H I depletion time in §3.4. We summarize our work in the last section.

Throughout this paper we assume a spatially flat concordance cosmology with $\Omega_m = 0.3$, $\Omega_\Lambda = 0.7$ and $H_0 = 70 \text{ km s}^{-1} \text{ Mpc}^{-1}$, unless otherwise specified.

2. Data

2.1. The low- z calibrating sample

We have calibrated the correlation between H I-to-stellar mass ratio (M_{HI}/M_*) and $NUV - r$ colour using a sample of 660 local galaxies. This is a subset of the low- z calibrating galaxies used in Zhang et al. (2009) that are required to have not only optical data from SDSS and H I emission observations from HyperLeda (Paturel et al. 2003), but also imaging in the NUV band from the GALEX surveys (Martin et al. 2005). The derived galaxy parameters needed for the calibration include H I gas mass (M_{HI}), stellar mass (M_*) and rest-frame magnitudes in the NUV and gri bands. The H I gas masses are taken from the HyperLeda catalogue following Zhang et al. (2009). Following the work of Wang et al. (2010), we have reprocessed both the NUV -band images from GALEX and the $ugriz$ -band images from SDSS for each of the galaxies to obtain better photometry than available from the GALEX and SDSS databases. In brief, we first register all the images to the frame geometry of the NUV image, then convolve the images to a common PSF of the NUV image, and finally, we perform the photometry measurements using the same position and aperture as in the SDSS image. We have corrected all the magnitudes for Galactic extinction, which is determined from the dust maps of Schlegel et al. (1998) with the extinction curves of Cardelli et al. (1989) with $R_V = A_V/E(B - V) = 3.1$ for the SDSS bands, implying that $A_\lambda/E(B - V) = 8.2$ for the NUV band (Wyder et al. 2007).

We use a Bayesian approach to estimate a stellar mass from the rest-frame colours for each galaxy in our sample, following Kauffmann et al. (2003) and Salim et al. (2005). A library of 25,000 Monte Carlo realizations of model star formation histories are generated between $0 < z < 0.5$ in regular bins of $\Delta z = 0.001$, using the population synthesis code of Bruzual & Charlot

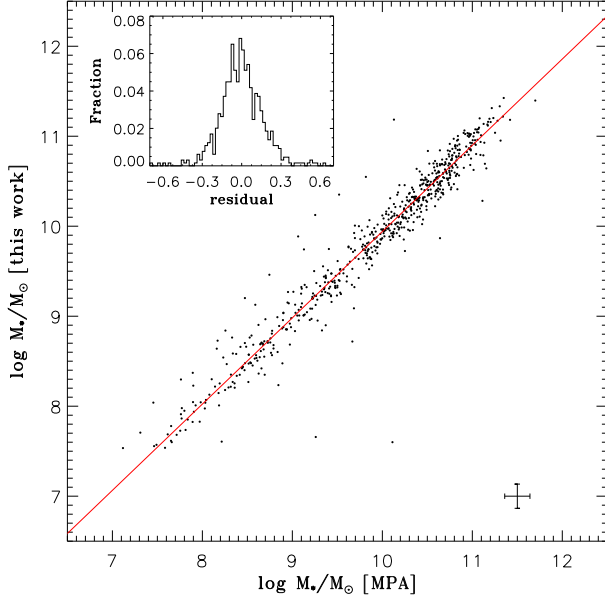


Fig. 1. Stellar masses estimated in this work for the galaxies in the low- z calibrating sample are compared to those from the MPA/JHU catalogues. The red line represents a linear fit to the data and the histogram of the residual of galaxies around the best-fit line is plotted in the inset.

(2003, BC03). Each star formation history is characterized with two components: an underlying continuous model with an exponentially declining star formation law plus random bursts superimposed on the continuous model. The models also have metallicities and dust attenuation uniformly distributed over wide ranges. The initial mass function (IMF) of Kroupa (2001) is adopted. For each galaxy we derive the probability distribution functions (PDFs) of the stellar mass and rest-frame magnitudes in different bands by comparing the observed spectral energy distribution (SED) to all the model SEDs that are in the closest redshift interval. In this procedure each model is weighted by $\exp(-\chi^2/2)$, where χ^2 is the goodness of fit of the model. We adopt the mean values of the PDFs as our estimates of these quantities. The SDSS *ugriz* SEDs are used when estimating the stellar masses, while the *NUV* magnitude is included additionally when estimating the rest-frame $g - i$ and $NUV - r$ colours. Our stellar mass estimates are in good agreement with those from the MPA/JHU SDSS DR4 database¹, as shown in Fig. 1.

2.2. DEEP2 galaxy sample

The high- z galaxy sample used in this work is based on the third data release (DR3; Newman et al. 2013) of the DEEP2 survey² and the K_s -band selected catalogue of Bundy et al. (2006)³. The DEEP2 Galaxy Redshift Survey (Davis et al. 2003) utilizes the DEIMOS spectrograph (Faber et al. 2003) on the Keck II telescope. Targets for the spectroscopic sample were selected from *BRI* photometry (Coil et al. 2004) taken with the 12k \times 8k mosaic camera on the Canada-France-Hawaii Telescope (CFHT). The images have a limiting magnitude of $R_{AB} \sim 25.5$. Since the R -band provides the highest signal-to-noise ratio (S/N) among all

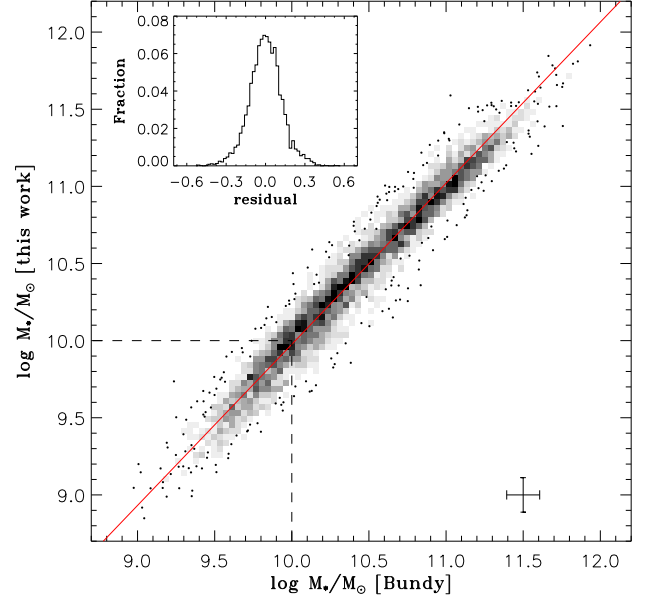


Fig. 2. Stellar masses estimated in this work for the DEEP2 galaxies are compared to those from Bundy et al. (2006). The red line represents a linear fit to the data and the histogram of the residual of galaxies around the best-fit line is plotted in the inset. Bundy et al. (2006) found that the spectroscopic sample in DEEP2 regions is incomplete below $M_* \sim 10^{10} M_\odot$.

the CFHT bands, the photometry in this band was used to select targets for spectroscopic observations with the DEEP2 spectrograph. The CFHT imaging covers four widely separated regions, with a total area of 3.5 deg^2 . In fields 2–4, the spectroscopic sample is pre-selected using $(B - R)$ and $(R - I)$ colours to eliminate objects with $z < 0.7$ (Davis et al. 2003). Colour and apparent magnitude cuts were also applied to objects in the first field, the Extended Groth Strip (EGS), but these were designed to down-weight low-redshift galaxies to select roughly equal number of galaxies below and above $z = 0.7$ (Willmer et al. 2006).

Based on the DEEP2 sample, Bundy et al. (2006) conducted an extensive imaging survey of all the DEEP2 fields with the Wide Field Infrared Camera (WIRC; Wilson et al. 2003) on the 5-metre Hale Telescope at Palomar Observatory. Using contiguously spaced pointings, the central third of fields 2 – 4 was mapped to a median 80% completeness depth greater than $K_{AB} = 21.5$, accounting for 0.9 deg^2 on the sky. The EGS field covers 0.7 deg^2 with varying but deeper depths. A stellar mass was estimated by Bundy et al. (2006) for each of their galaxies. First, a K_s -band mass-to-light ratio M_*/L_{K_s} was obtained by comparing the observed *BRICKs* SED to a grid of 13,440 synthetic SEDs constructed from BC03 spanning a range of star formation histories, ages, metallicities and dust content. The stellar mass of the galaxy is then given by scaling M_*/L_{K_s} to the K_s -band luminosity measured from the total K_s -band magnitude and the DEEP2 spectroscopically-measured redshift.

In this work, we make use of the galaxy sample from Bundy et al. (2006), which consists of 7,222 galaxies with redshifts in the range $0.75 \leq z \leq 1.40$, redshift quality parameters $z_{\text{quality}} \geq 3$ and K_s -band magnitudes $K_s \leq 20$. For consistency, we estimate a stellar mass for each of the galaxies using the same method we used above for the low- z calibrating sample. The observed SED used for the estimation involves photometry

¹ <http://www.mpa-garching.mpg.de/SDSS/DR4/>

² <http://deep.berkeley.edu/>

³ <http://deep.berkeley.edu/~kbundy/>

in B , R , I and K_s bands. Our stellar mass estimates are compared to those obtained by Bundy et al. (2006) in Fig. 2, which are in good agreement with no obvious systematic difference. We have also estimated the rest-frame $g - i$ and $NUV - r$ colours for the galaxies using the same method.

Following previous studies (e.g. Bundy et al. 2006; Chen et al. 2009) we weight each galaxy in our DEEP2 sample to correct for incompleteness when performing statistical analyses:

$$W = \frac{\kappa}{V_{\max}}, \quad (1)$$

where κ accounts for incompleteness resulting from the DEEP2 colour selection and redshift success rate. The “optimal” weighting model of Willmer et al. (2006) is used to estimate κ , which accounts for the redshift success rate for red and blue galaxies in different ways. We adopt the luminosity-dependent colour divider employed by van Dokkum (2008) for classifying the galaxies into red and blue:

$$U - B = -0.032(M_B + 21.52) + 0.454 - 0.25, \quad (2)$$

where the rest-frame $U - B$ colour and the B -band absolute magnitude M_B are obtained above using our Bayesian approach. The $U - B$ histogram and the M_B versus $U - B$ diagram are shown in Fig. 3, for two successive redshift intervals: $0.75 < z < 1$ and $1 < z < 1.4$.

The second factor V_{\max} is defined as the maximum volume over which the galaxy would be included in the sample, accounting for the fact that faint galaxies are not detected throughout the entire survey volume in a flux-limited survey. Following Willmer et al. (2006), the V_{\max}^i for a galaxy i can be calculated as:

$$V_{\max}^i = \int_{\Omega} \int_{z_{\min,i}}^{z_{\max,i}} \frac{d^2V}{d\Omega dz} dz d\Omega \quad (3)$$

where z and Ω are the redshift and the solid angle, respectively. The redshift limits $z_{\min,i}$ and $z_{\max,i}$ are imposed either by the limits of the redshift bin being dealt with or by the apparent magnitude limits of the DEEP2 sample. More details can be found in Willmer et al. (2006).

We have estimated stellar mass functions for the two redshift bins, which are plotted in Fig. 4 as diamonds connected by solid lines, and these are compared to the estimates obtained by Bundy et al. (2006), shown as crosses connected by dashed lines. The two estimates are almost identical, indicating that we have correctly calculated the weights for incompleteness correction. For the mass function estimates (and the H I mass functions in the next section) we have used 5,372 out of the 7,222 galaxies with $M_* > 10^{10} M_{\odot}$. Below this mass, the DEEP2 sample becomes significantly incomplete (Bundy et al. 2006). The errors on the stellar mass functions are estimated using the 1σ scatter in the measurements of the four DEEP2 fields.

For one of the four DEEP2 fields, the Extended Groth Strip (EGS), SFR measurements of galaxies have been carried out by Barro et al. (2011) using SEDs covering the wavebands from UV to FIR, including the IRAC 3.5 and 4.6 μm bands. About 2000 blue galaxies in the EGS field in our sample have SFR measured in this way.

3. Results

3.1. The H I mass fraction estimator

The H I-to-stellar mass ratio is strongly correlated with galaxy parameters such as optical colours, $NUV - r$ colour, μ_* , R_{90}/R_{50}

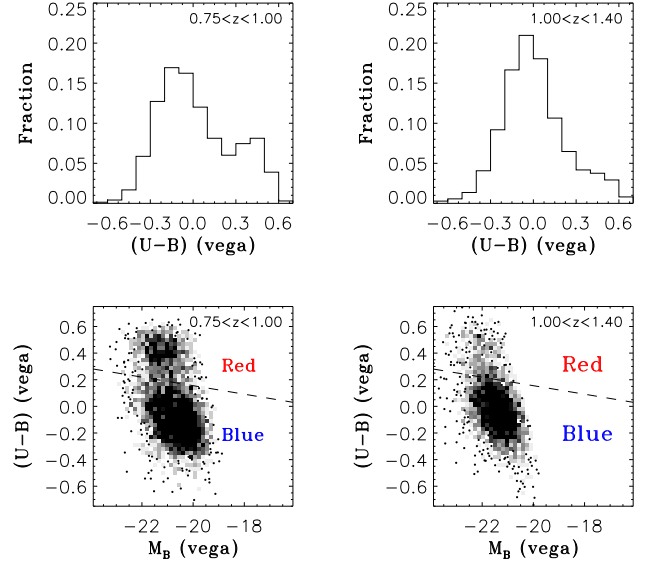


Fig. 3. Histograms of the Rest-frame $U - B$ colour (top panels) and diagrams of $U - B$ vs. B -band absolute magnitude (lower panels) are shown for DEEP2 galaxies in two successive redshift intervals: $0.75 < z < 1$ (left panels) and $1 < z < 1.4$ (right panels). The dashed line in the lower panels is the luminosity-dependent colour divider employed by van Dokkum (2008), which is used in this work to classify our galaxies into red and blue populations. Magnitudes plotted in this figure are in the Vega system.

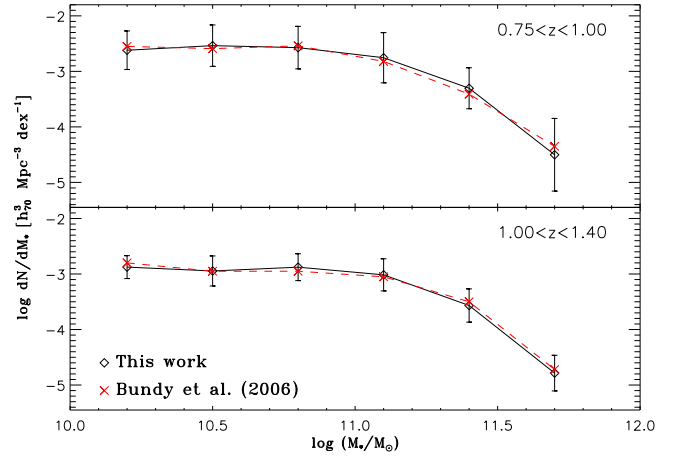


Fig. 4. Stellar mass functions at the two redshift intervals as indicated are plotted in black diamonds, and are compared to the measurements from Bundy et al. (2006) plotted in red crosses.

and M_* , with a typical scatter of ~ 0.35 dex. The relation between M_{HI}/M_* with the combination of two or more parameters is tighter than the relation between M_{HI}/M_* with a single parameter, with a typical scatter of ~ 0.30 dex (Zhang et al. 2009; Li et al. 2012; Catinella et al. 2010). Unlike Zhang et al. (2009), we take the combination of $NUV - r$ and μ_* , instead of optical colour and μ_* in this work, because of two considerations: 1) As we see from Fig. 5, low redshift galaxies show very narrow dynamic range in $g - i$ with $1 \lesssim g - i \lesssim 1.2$, but $NUV - r$ spans a broader range of values ($3.5 \lesssim (NUV - r) \lesssim 6$). This is more clearly seen in the right-hand panel of the same figure, where $g - i$ is plotted against $NUV - r$. When $NUV - r$ increases above

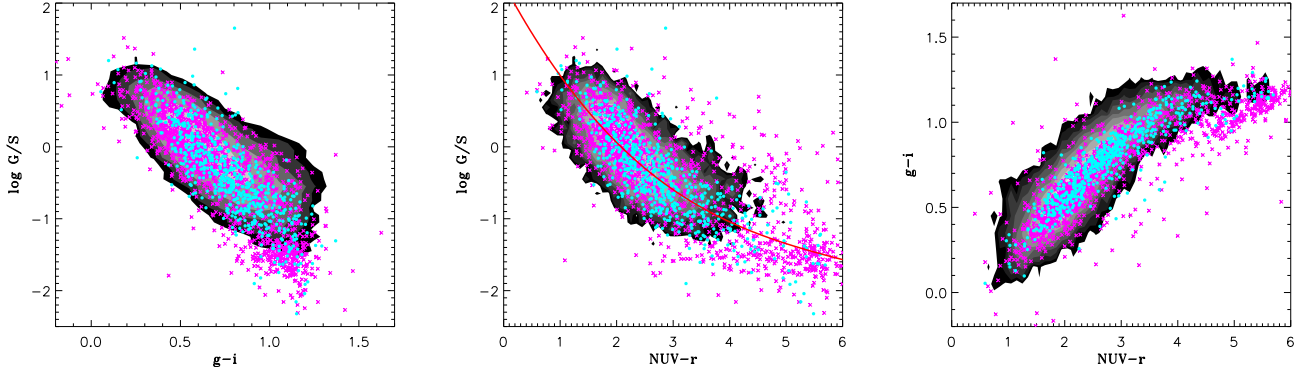


Fig. 5. Correlation of H I-to-stellar mass ratio (M_{HI}/M_*) with $g-i$ (left) and $NUV-r$ (middle) for the low- z calibrating sample. The best-fit models are plotted as a solid red line (see the text for detailed description). The right-hand panel shows the relation between $g-i$ and $NUV-r$ for the same set of galaxies. The low- z calibrating sample are plotted as cyan filled dots, the RESOLVE sample are plotted as magenta crosses, while the final ALFALFA 100 per cent catalogue ($\alpha.100$) are shown as black-and-white contours in each panel.

~ 3.5 , $g-i$ doesn't increase any more and is fairly constant at $g-i \approx 1.1$, suggesting that $NUV-r$ is more sensitive than $g-i$ to the atomic gas content for the most H I-poor galaxies. This is consistent with the finding of Catinella et al. (2010) that, among the four parameters considered (M_* , μ_* , R_{90}/R_{50} , $NUV-r$), the $NUV-r$ colour was the one most tightly correlated with the H I-to-stellar mass ratio. 2) for the DEEP2 galaxies at $z \sim 1$, their rest-frame NUV magnitude is redshifted to the optical band, and in this case the k -correction is relatively small and can be estimated more reliably than in the case where the g magnitude is used.

The physical reason why H I is better predicted by $NUV-r$ colour likely arises from the fact that the ultra-violet emission from a galaxy traces the light from young stars in low density, extended gas in the outer disks of galaxies that has not been absorbed by dust. The molecular gas traced by CO emission is, on the other hand, known to be tightly correlated with the infrared luminosity of the galaxy (Young et al. 1984; Sanders & Mirabel 1985). This analysis will not address the molecular content of the galaxies in our sample.

We have checked the results of the low- z calibrating sample using more recent data from two larger H I catalogues. The first one is the REsolved Spectroscopy of a Local Volume (RESOLVE⁴) sample, which is completed in baryonic mass (defined as $M_{\text{bary}} = M_* + 1.4M_{\text{HI}}$) down to dwarfs of $\sim 10^9 M_\odot$ (Eckert et al. 2015; Stark 2016). The second one is the final ALFALFA 100 per cent catalogue ($\alpha.100$ ⁵) (Jones et al. 2018; Haynes et al. 2018). The galaxies with signal-to-noise lower than 5 are excluded from this sample. The RESOLVE and the $\alpha.100$ samples are shown in Fig. 5 as magenta crosses and black-and-white contours, respectively. Note that for these two samples, the colours and the stellar masses used here are obtained from the NASA-Sloan Atlas (NSA) catalogue (v1_0_1⁶), and the colours are corrected for Galactic extinction. As a result, about 1,500 RESOLVE galaxies and about 13,000 $\alpha.100$ galaxies are used to compare with the low- z calibrating sample. We can see that although the low- z calibrating sample is small, it follows the same trend with the RESOLVE and the $\alpha.100$ samples. This confirms that the estimator derived using low- z calibrating sample is robust.

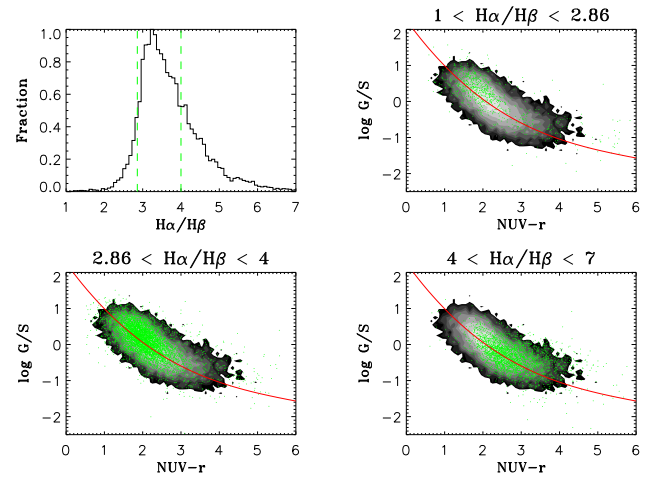


Fig. 6. The effect of dust attenuation to the relation between M_{HI}/M_* and $NUV-r$ colour. The distribution of $H\alpha$ -to- $H\beta$ ratio of the $\alpha.100_{\text{spec}}$ sample is shown in the top-left panel. The green dashed lines indicate the division of the sample into three subsamples. In the other panels, the three subsamples are shown as green dots in M_{HI}/M_* vs. $NUV-r$ diagram. Similar to the middle panel in Fig. 5, the black-and-white contours are the final ALFALFA 100 per cent catalogue ($\alpha.100$), while solid red line is the relation described in Eq. 4. As can be seen, galaxies of different dust content are shifted along the derived relation, not displaces away from it.

We use a polynomial function to represent the observed non-linear relation of M_{HI}/M_* versus $NUV-r$,

$$\log G/S = a_0 + a_1(NUV-r) + a_2(NUV-r)^2 + a_3(NUV-r)^3, \quad (4)$$

plotted as a red line in the middle panel of Fig. 5. Here the best-fit parameters are $a_0 = 2.26432$, $a_1 = -1.46308$, $a_2 = 0.202311$ and $a_3 = -0.0108242$. The 1σ scatter of the galaxies around this relation is 0.36 dex.

We have explored possible systematic effects due to dust attenuation on the correlation between H I gas fraction and $NUV-r$ colour. $H\alpha$ -to- $H\beta$ decrement can be used as an indicator of dust attenuation, for which higher values of $H\alpha/H\beta$ indicate higher dust attenuation values. We obtain a sample of $\sim 10,000$ galaxies (hereafter $\alpha.100_{\text{spec}}$ sample) which have high signal-to-ratio ($S/N > 3$) detection of $H\alpha$ and $H\beta$ emission lines, by

⁴ <http://resolve.astro.unc.edu>

⁵ <http://egg.astro.cornell.edu/alfalfa/>

⁶ <https://data.sdss.org/sas/dr16/sdss/atlas/v1/>

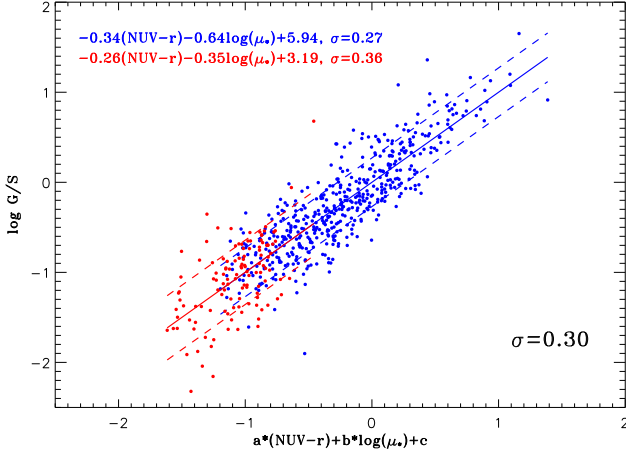


Fig. 7. The relation between H I gas fraction and the linear combination of $NUV - r$ colour and stellar surface mass density (μ_*) in the SDSS-z band. The low- z calibrating sample has been divided into two subsamples according to $NUV - r$ colour: the red points are galaxies with $(NUV - r) > 3.5$, while the blue points are galaxies with $(NUV - r) < 3.5$. The fitting parameters are labeled at top-left of the figure.

cross-matching the $\alpha.100$ sample with SDSS DR8 spectroscopic sample. We note that all galaxies on the star-forming main sequence in SDSS have $H\alpha$ and $H\beta$ with this S/N or higher. We divide the sample into three subsamples according to the $H\alpha$ -to- $H\beta$ ratio as shown in the top-left panel in Fig. 6, and we plot these subsamples in the H I gas fraction and $NUV - r$ colour diagram in the other three panels. As in the middle panel of Fig. 5, the final ALFAFA 100 per cent catalogue ($\alpha.100$) is shown as black-and-white contours for comparison. The galaxies having $H\alpha$ and $H\beta$ detections are over-plotted as green dots, with the cuts noted on the top of each panel. The solid red line is the relation described in Eq. 4. It is found that the galaxies with higher dust attenuation have redder $NUV - r$ colours and lower H I gas fractions. However, they still follow the correlation between H I gas fraction and $NUV - r$ colour. We conclude that it is safe to apply the estimator to galaxies with various dust attenuation values.

Fig. 7 shows the relationship between H I-to-stellar mass ratio, G/S , and a linear combination of $NUV - r$ and stellar surface mass density μ_* , defined as $0.5M_*/R_{50}^2$, where M_* is the stellar mass of the galaxy and R_{50} is its z-band half light radius in units of kpc, for the galaxies in the low- z calibrating sample. This estimator could be expected to exhibit less scatter than one based on $NUV - r$ colour alone if the surface density of the atomic gas is well correlated with the surface density of the stars in galaxies. In practice, the H I often extends far beyond the disk traced in the optical light. Wang et al. (2013) show that there is a factor of ~ 1.5 scatter in ratio between H I size and optical size at fixed stellar mass, implying a factor of 2 or more scatter in surface density. We find that the estimator that includes μ_* has a scatter around the one-to-one line of 0.30 dex. We can obtain somewhat tighter results if we fit separate relations for galaxies with $(NUV - r) > 3.5$ and $(NUV - r) < 3.5$. The scatter of blue and red galaxies around their separate relation is 0.27 and 0.36 dex, respectively. The higher scatter for redder galaxies likely occurs because these galaxies contain more dust and a higher fraction of their total gas content is in molecular rather than atomic form.

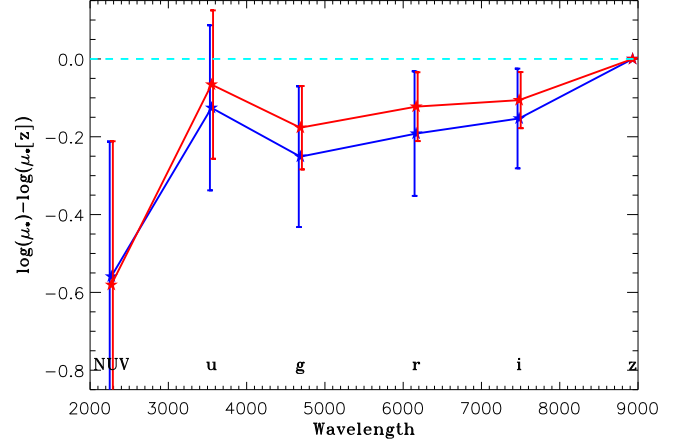


Fig. 8. The difference of μ_* in GALEX- NUV , $sdss-u$, g , r , i bands with that in $sdss-z$ band. As in Fig. 7, the red and blue colours represent galaxies with $(NUV - r) > 3.5$ and $(NUV - r) < 3.5$, respectively.

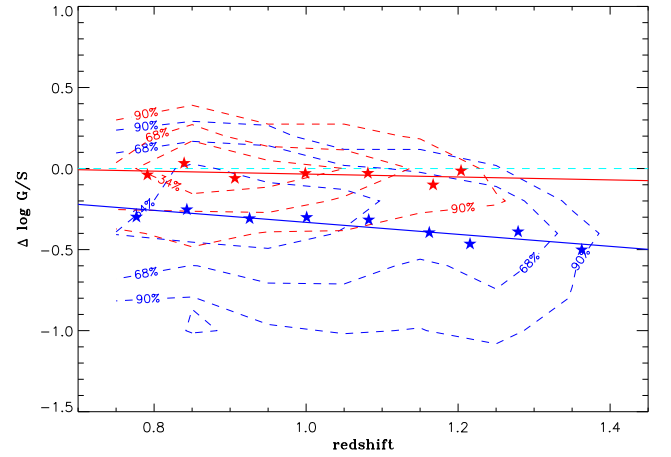


Fig. 9. The difference between G/S estimated from $NUV - r$ and μ_* and G/S estimated from $NUV - r$ only as function of redshift. The median value in each redshift bin and the linear fitting results of these median values are shown as star and solid line, respectively. The contours enclose 34, 68, and 90% of the sample. Similar to Fig. 7, the red and blue colour represent galaxies with $(NUV - r) > 3.5$ and $(NUV - r) < 3.5$, respectively.

This estimator cannot be applied into the whole high- z samples directly, because only one of the four DEEP2 fields, the EGS region, has half-light radius determined for each galaxy from HST observations. Before we apply the estimator to the EGS galaxies, we notice the fact that the HST half-light radius is determined in the I -band with effective wavelength of 8140 Å, corresponding to a rest-frame wavelength ranging from 3391 Å to 4651 Å for our galaxies. However, the μ_* for the low- z calibrating sample is obtained from the SDSS z -band at 8931 Å. As shown in Fig. 8, the surface mass density μ_* of galaxies changes from band to band due to the wavelength dependence of their half-light radii. In order to take into account this effect, we use the median difference in $\log \mu_*$ shown in the figure to make a correction to μ_* for galaxies in the EGS. Then for galaxies in the EGS region, we compare the gas fractions estimated from the linear combination of $NUV - r$ and μ_* with the gas fractions given by $NUV - r$ only, and find systematic differences that de-

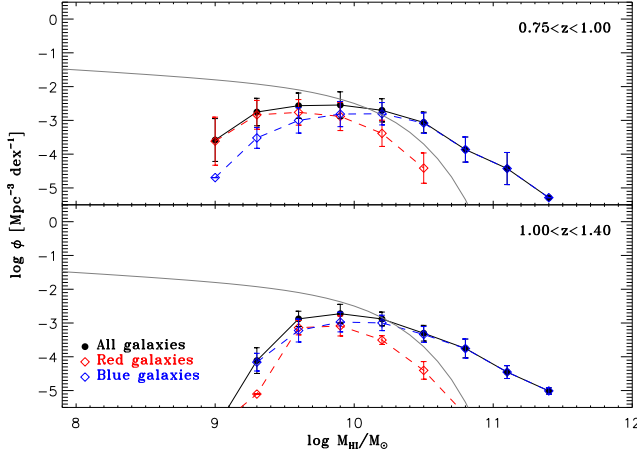


Fig. 10. H I mass functions estimated from the DEEP2 for the two redshift intervals as indicated are plotted in black solid circles connected by a solid line for the whole sample, and in red (blue) diamonds connected by a dashed line for the red (blue) galaxy subsamples. For comparison, the HIMF at $z = 0$ from α_{100} is shown as grey solid lines.

pend on redshift as shown in Fig. 9. For red and blue galaxies, the gas fraction taking into account μ_* is smaller by 0–0.1 and 0.2–0.5 dex, respectively.

In summary, in this section we have demonstrated that among the quantities we have access to, the combination of $NUV - r$ colour stellar surface density yields the best predictor for H I mass fraction for blue galaxies in particular. Use of a single colour such as $NUV - r$ leads to inaccurate predictions, depending on the weighting between red and blue galaxies in the sample. We show that a separate calibration for the two populations is necessary to obtain accurate estimates of the high-mass end of the HIMF and the cosmic H I mass density. In this analysis, we apply the median difference, shown in the red/blue stars and lines in the Fig. 9, to correct the gas fraction for all the galaxies in our DEEP2 sample. We note that our analysis in the following sections does not include any estimate of the molecular gas content of the galaxies and this component may have very different scaling relations than the atomic gas.

3.2. H I mass function at $z \sim 1$

Applying the H I mass fraction estimator obtained above, we have estimated an H I gas mass for each of the galaxies in the DEEP2 sample. The first statistic that we have obtained from this data is the H I mass function, which quantifies the co-moving number density of galaxies as a function of their H I mass. This statistic has not been estimated previously at these high redshifts. Specifically, we have estimated the HIMF for two successive redshift intervals, one below and one above $z = 1$. These are shown in Fig. 10 as black solid circles connected by a solid line. When estimating the HIMFs, we have corrected for sample incompleteness in the same way as described above for estimating the stellar mass functions. We have restricted ourselves to galaxies with $\log(M_*/M_\odot) > 10$ for the same reason as explained above. The errors on the HIMFs are estimated from the 1σ scatter of the HIMFs of the four separate fields of the DEEP2.

For each redshift interval, we have also estimated an HIMF for the subset of galaxies with either red or blue $U - B$ colours, classified using the colour divider in equation (2). The estimates are also shown in Fig. 10. For comparison, the HIMF of the local

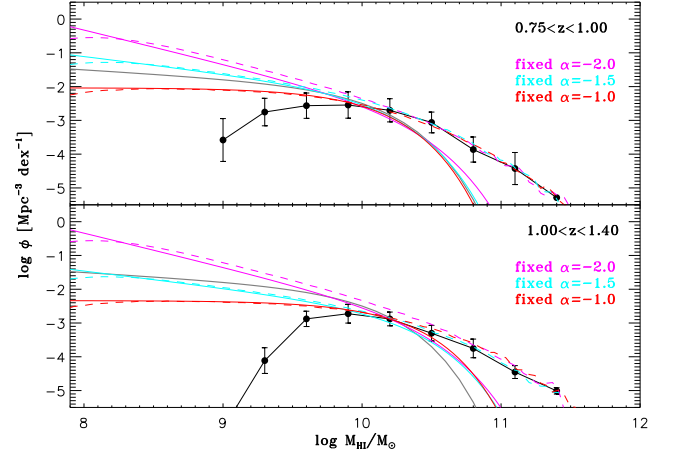


Fig. 11. Schechter function fits with the slope fixed to $\alpha = -2, -1.5, -1.0$ are shown as magenta, cyan and red dashed lines. During fitting, a 0.35 dex scatter of $\log(M_{\text{HI}})$ is adopted. The corresponding Schechter functions without scatter in $\log(M_{\text{HI}})$ are shown as solid lines.

Universe obtained by Jones et al. (2018) from the final catalogue of the ALFALFA (α_{100}) is plotted as a grey solid line in the same figure.

We see that at H I masses above $\sim 10^{10} M_\odot$, the abundance of galaxies decreases slowly with increasing H I mass before it drops rapidly at masses above $\sim 10^{11} M_\odot$. This behaviour is similar to the luminosity functions and stellar mass functions found in the local Universe, which can usually be described by a Schechter function. At masses below $\sim 10^{10} M_\odot$, the HIMFs also decreases, and this should be attributed to the fact that the galaxies with stellar mass below $10^{10} M_\odot$ are not included in the measurement. For this reason, the HIMFs presented here can only be regarded as lower limits of the number density of galaxies with H I masses lower than $\sim 10^{10} M_\odot$. Hence in the following analysis, we only fit a Schechter function to the HIMFs at H I masses above $10^{10} M_\odot$.

We note that the errors on the H I masses can affect the shape of the HIMFs, in particular at the high mass end. Given that the scatter in our estimates of the gas fraction $\log(M_{\text{HI}}/M_*)$ and in the stellar mass $\log(M_*)$ is 0.30 dex (see Fig. 2) and 0.11 dex (see Fig. 7), the scatter of H I gas mass $\log(M_{\text{HI}})$ is estimated as 0.32 dex. Considering the uncertainties of the corrections described in §3.1, a total error in $\log(M_{\text{HI}})$ of 0.35 dex is assumed. We then fit a Schechter function to the HIMFs at H I masses above $10^{10} M_\odot$, by considering the scatter of $\log(M_{\text{HI}})$ with value of 0.35 dex. We note that the flat slope of the HIMF at low masses in highly uncertain because of the extrapolation to low masses. We have tried to fit to the HIMF measurements with the slope parameter fixed to three different values: $\alpha = -1, -1.5$ and -2 , and plot the best-fit functions as dashed red, cyan and magenta lines in Fig. 11. As can be seen from the figure, fitting to the HIMFs with different Schechter function slopes cannot effectively constrain the slope parameter at the low-mass end. At the high-mass end, the shape is well constrained, and consistent with no evolution at the bright end.

3.3. H I mass density at $z \sim 1$

The second quantity that we have obtained from our data is the cosmic H I mass density, Ω_{HI} , which is the volume density of H I mass contained in galaxies at given redshift normalized by

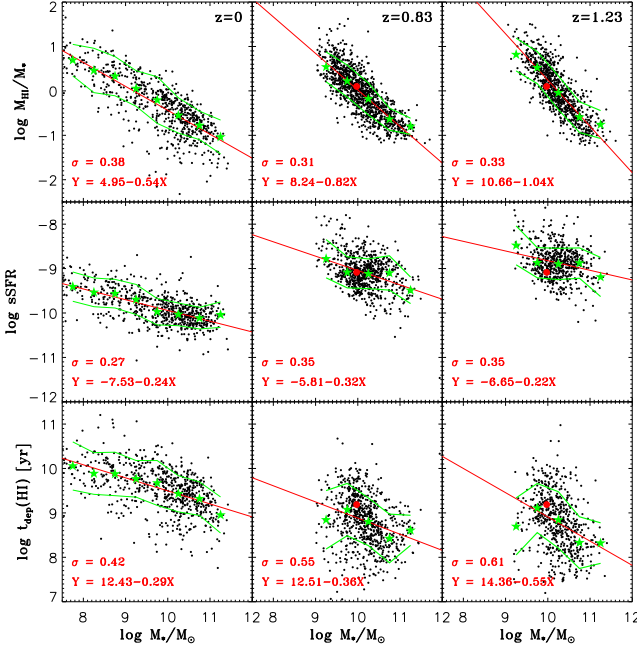


Fig. 12. The H I-to-stellar mass ratio (M_{HI}/M_* ; top panels), specific star formation rate (SFR/M_* ; second row of panels) and the H I gas depletion time (M_{HI}/SFR ; bottom panels) are plotted as a function of stellar mass, for the low- z calibrating sample (left) and the DEEP2 galaxies at the two higher redshifts (center and right panels). The small black dots are for the low- z calibrating sample or the blue galaxies at high redshifts, and the red line in each panel shows the best fitting with a linear relation. The stars and the two solid lines plotted in green show the median and 1σ scatter for a number of stellar mass bins. For comparison, the mean measurements of star-forming galaxies at redshift $z \sim 1$ by Chowdhury et al. (2020) are plotted as red filled circles.

the critical density of matter in the universe. Because of large uncertainties for the slope at the low-mass end, we did not try to estimate the total Ω_{HI} from the best-fit Schechter functions shown in Fig. 11. Instead, we measure the lower limits of Ω_{HI} by directly integrating the HIMFs, using galaxies with $M_* > 10^{10} M_\odot$. The scatter among the four DEEP2 fields is adopted as the 1σ uncertainty on the measurement. We derive lower limits $\Omega_{\text{HI,limit}} = (2.44 \pm 0.76) \times 10^{-4} h_{70}^{-1}$ and $(1.66 \pm 0.54) \times 10^{-4} h_{70}^{-1}$ for the two redshift bins. We note that the mean measurement of $\Omega_{\text{HI,limit}} \sim 2.1 \times 10^{-4} h_{70}^{-1}$ at $z \sim 1$ is comparable with that of $\Omega_{\text{HI,Bright}} = (2.31 \pm 0.58) \times 10^{-4} h_{70}^{-1}$ by directly stacking of 21-cm signatures of blue, star-forming galaxies with $M_B \leq -20$ at similar redshifts in the DEEP2 fields (Chowdhury et al. 2020).

3.4. Correlations between H I mass fraction, stellar mass, specific star formation rate, and H I depletion time

In this subsection we study the correlation of the H I gas content of the galaxies at $z \sim 1$ with their star formation rate (SFR) using galaxies from the the Extended Groth Strip (EGS), for which SFR measurements of galaxies are available. The SFR measurements range from 1 to $3 M_\odot \text{yr}^{-1}$, with a median value of $1.2 M_\odot \text{yr}^{-1}$. In Fig. 12 and 13 we use this sample (again, split into two subsamples by redshift), as well as the low- z calibrating sample, to examine the correlations between the specific SFR, the H I mass fraction, and the quantity M_{HI}/SFR . We note that M_{HI}/SFR should be regarded as a lower limit to the actual time taken for the H I gas to be depleted. In low redshift galaxies,

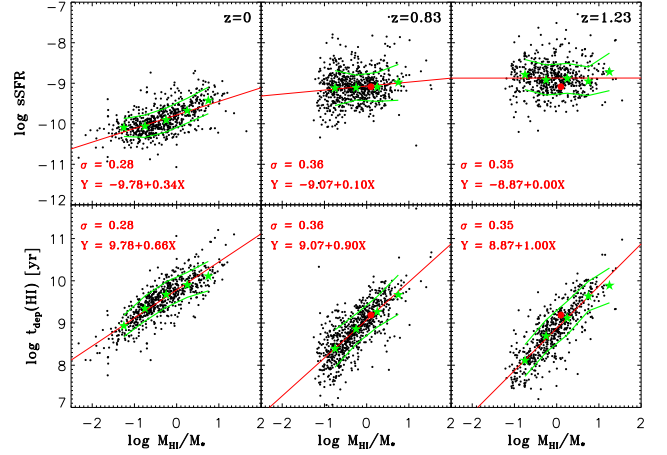


Fig. 13. Correlations of specific star formation rate and H I gas depletion time with H I-to-stellar mass ratio are plotted for the same sets of galaxies with the same symbols/lines as in the previous figure.

most of the H I gas is often well outside the star-forming disk in a dynamically stable configuration. Some of this gas may be a reservoir for future star formation in the galaxy, but the timescale for consumption of the gas will depend on uncertain parameters such as gas inflow rates. At high redshifts, gas inflow rates are higher, the dynamical timescales of galaxies are shorter and extended gas reservoirs may be converted into stars more quickly. Therefore one might expect to see better correlation between the star formation rate and the H I gas content at high redshift. Our results, however, indicate that this is not true.

The top three panels in Fig. 12 show the distribution of galaxies in the $\log M_{\text{HI}}/M_*$ versus $\log M_*$ plane. The low- z calibrating sample shows a tight, nearly-linear relation with a slope of -0.54 and a 1σ scatter of 0.38 dex. A similarly tight relation is seen at $z = 0.83$ and $z = 1.23$, with scatter 0.31 and 0.35 dex. The correlation seems to steepen to higher redshifts; fitting to the data with a linear relation leads to slope parameters of -0.82 and -1.04 for the two high- z samples compared to -0.54 for the low- z sample. To take into account the effect of incompleteness, we also fit the data weighted by $1/V_{\text{max}}$. The resulting slopes are -0.72 and -0.93 . The normalization of the correlation also increases with redshift. At stellar mass of $10^{11} M_\odot$ the average H I-to-stellar mass ratio is 0.1 at $z \sim 0$, and this increases by a factor of 3–4, up to ~ 0.3 at $z \sim 0.8$ and ~ 0.4 at $z \sim 1.2$. The increase is even more dramatic at smaller stellar masses, e.g. by a factor of 4–12 at $M_* = 10^{10} M_\odot$. These results show that distant galaxies are on average much more H I-rich than local galaxies, and the slope of the relation between H I gas mass fraction and stellar mass also evolves with redshift. We have checked the nature of the galaxies with $M_{\text{HI}} > 10^{10} M_\odot$ in the EGS field, and have found that their half-light radii in HST I-band vary from 20 to 90 kpc, and the surface mass density of H I gas using this size estimate is about $37 M_\odot \text{pc}^{-2}$.

In the middle panels we reproduce the star formation sequence by showing the $\log(\text{SFR}/M_*)$ versus $\log M_*$ planes. There is a similar increase in the normalization of the relation. Interestingly, the relation between sSFR and stellar mass shows larger scatter at $z \sim 1$ than the relation between H I gas mass fraction and stellar mass. We note that the molecular gas fraction also increases by a factor of 3–4, from $z = 0$ to $z \sim 0.8$ and $z \sim 1.2$, according to the evolution trend of $f_{\text{mol-gas}} \propto (1+z)^2$ (Geach et al. 2011; Carilli & Walter 2013).

In the bottom panels of Fig. 12, we show the correlation of M_{HI}/SFR with stellar mass for the same sets of galaxies. This quantity yields rather short timescales at all redshifts probed (0.5–2 Gyr at $z \sim 1$ and a factor only ~ 2 larger at $z \sim 0$), but as we have noted, these are likely lower limits to the actual time taken for the gas to be consumed. More interesting is that this quantity exhibits very weak redshift evolution, similar to the H I gas and star formation main sequences discussed above. This indicates that the star formation main sequence may simply be a natural result of the cosmic evolution of the available gas reservoir in galaxies. Furthermore, it is also seen that M_{HI}/SFR at fixed stellar mass shows a huge scatter, ~ 0.6 dex at $z \sim 1$ and ~ 0.4 dex in the local Universe, implying a weak correlation between M_{HI} and SFR, as expected for a gas component that is not directly linked with the star formation in the galaxy population.

In the upper panels of Fig. 13, we plot the galaxies in the plane of $\log(\text{SFR}/M_*)$ versus M_{HI}/M_* . At $z \sim 1$ the sSFR is confined to a narrow range, again reflecting the tightness of the star formation sequence, while M_{HI}/M_* spans a much wider range. This causes the quantity M_{HI}/SFR to be tightly correlated with M_{HI}/M_* , as shown in the lower panels of the same figure.

The scaling relations shown in Figures 13 and 14 are best interpreted in conjunction with either semi-analytic models of galaxy formation that model the spatial distribution of the gas (e.g. Fu et al. 2010; Lagos et al. 2011; Popping et al. 2014; Xie et al. 2017) or cosmological hydrodynamical simulations with sufficient (1 kpc or better) resolution to resolve the formation of galaxy disks over the same mass scales as in our sample (e.g. Vogelsberger et al. 2014; Schaye et al. 2015; Pillepich et al. 2018). These models follow the cooling and condensation of gas in galaxy halos. The formation of molecular gas is often incorporated as post-processing step (e.g. Diemer et al. 2019). Comparisons with H I scaling relations such as those presented in this section then constrain gas accretion and condensation processes in the models, which depend sensitively on processes such as supernova and AGN feedback.

4. Conclusions

Using the rest-frame near-ultraviolet (NUV)-optical colour, $NUV-r$, as a proxy for the H I-to-stellar mass ratio, M_{HI}/M_* , we have estimated the H I gas mass for a sample of $\sim 7,000$ galaxies in the DEEP2 survey with redshifts in the range $0.75 < z < 1.4$ and stellar masses above $\sim 10^{10} M_\odot$. The correlation between M_{HI}/M_* and $NUV-r$ is calibrated with a sample of 660 galaxies in the local Universe that have optical and NUV photometry from SDSS and GALEX, as well as 21-cm emission data from HyperLeda. With these H I mass estimates, we have calculated H I mass functions (HIMFs) and cosmic H I gas densities (Ω_{HI}), and we have investigated the correlations between the specific star formation rate (SFR/M_*), the H I-to-stellar mass ratio (M_{HI}/M_*) and the H I gas depletion time ($t_{\text{dep}}(\text{HI}) \equiv M_{\text{HI}}/\text{SFR}$).

Our main conclusions can be summarized as follows.

- For galaxies with stellar masses above $\sim 10^{10} M_\odot$, the HIMF at $z \sim 1$ is quite similar to the local HIMF, while the low-mass end slope cannot be constrained due to the lack of low stellar mass galaxies in our sample.
- Integrals of our HIMFs suggest the lower limit of the H I mass density at $z \sim 1$ to be $\Omega_{\text{HI,limit}} \sim 2.1 \times 10^{-4} h_{70}^{-1}$, which is significantly smaller than the estimates obtained by other authors based on DLAs at the same redshift. However, our work confirms the result of Kanekar et al. (2016), that massive star-forming galaxies do not dominate the neutral gas at $z \sim 1$.

- Galaxies with $M_* \sim 10^{11} M_\odot$ at $z = 1$ have large H I gas fractions, which are about 3–4 times higher than local galaxies, indicating the neutral gas fraction evolves from $z = 1$ to the present epoch. It is found that the slope of the correlation between H I gas fraction and stellar mass also has a modest evolution with redshift.
- The quantity M_{HI}/SFR exhibits very large scatter, and the scatter increases from a factor of 5–7 at $z = 0$ to factors in close to a hundred at $z = 1$. This implies that there is no relation between H I gas and star formation in high redshift galaxies. The H I gas must be linked to cosmological gas accretion processes.

As discussed previously, all the results obtained in this work rely on the assumption that the same scaling relation between H I mass fraction and NUV-optical colour applies at higher redshifts. Although our measurements of gas fraction and cosmic H I mass density are consistent with that derived from co-adding method or Mg II absorbers, it would be very useful to obtain small samples of galaxies with H I measured at $z = 1$ to validate that the scaling relations hold at this redshift. This goal should be achieved with the help of the future radio telescopes such as the next-generation VLA (ngVLA) and the Square Kilometre Array (SKA). From the linear fitting relations between M_{HI}/M_* and M_* for the galaxies in two high- z bins in Fig. 12, a lower limit of $M_{\text{HI}} \sim 2.7 \times 10^{10} M_\odot$ is required to derive the scaling relations covering a wide range of M_* from 10^9 to $10^{11} M_\odot$ at $z \sim 1$. Using the equation $\frac{M_{\text{HI}}}{M_\odot} = 2.356 \times 10^5 D_{\text{Mpc}}^2 \times S_{21}$, where D_{Mpc} is the distance to the galaxy in Mpc, the integrated flux density detection threshold $S_{21,\text{th}}$ can be calculated as $2.6 \times 10^{-3} \text{ Jy km s}^{-1}$. Taking this threshold, sufficient number of galaxies can be detected at $z \sim 1$ according to the simulations of SKA detection rates (Obreschkow et al. 2009).

Acknowledgement

W.Z. is grateful to MPA for hospitality when this work was being completed. W.Z. deeply appreciate that Cheng Li has given a lot of guidance and recommendations for this work. W.Z. thanks Kevin Bundy for kindly sharing the catalogue of K_s magnitude and stellar mass. W.Z. thanks Zheng Zheng, and Qi Guo for helpful suggestions. This work is supported by the Joint Research Fund in Astronomy (No. U1531118) under cooperative agreement between the National Natural Science Foundation of China (NSFC) and Chinese Academy of Sciences (CAS). This work is also sponsored by NSFC (No. 12090041, 12090040, 10903011, 11173045, 11733006), the National Key R&D Program of China grant No. 2017YFA0402704, and the Guangxi Natural Science Foundation (No. 2019GXNSFFA245008). J.F. acknowledges the support by the Youth innovation Promotion Association CAS and Shanghai Committee of Science and Technology grant No. 19ZR1466700 and the support by the Joint Research Fund in Astronomy (No. U1531123). This work has made use of data from the SDSS and SDSS-II, and the HyperLeda database.

References

- Barro, G., Pérez-González, P. G., Gallego, J., et al. 2011, *ApJS*, 193, 30
- Bruzual, G. & Charlot, S. 2003, *MNRAS*, 344, 1000
- Bundy, K., Ellis, R. S., Conselice, C. J., et al. 2006, *ApJ*, 651, 120
- Cardelli, J. A., Clayton, G. C., & Mathis, J. S. 1989, *ApJ*, 345, 245
- Carilli, C. L. & Walter, F. 2013, *ARA&A*, 51, 105
- Catinella, B., Haynes, M. P., Giovanelli, R., Gardner, J. P., & Connolly, A. J. 2008, *ApJ*, 685, L13

- Catinella, B., Saintonge, A., Janowiecki, S., et al. 2018, *MNRAS*, 476, 875
- Catinella, B., Schiminovich, D., Kauffmann, G., et al. 2010, *MNRAS*, 403, 683
- Chang, T.-C., Pen, U.-L., Bandura, K., & Peterson, J. B. 2010, 466, 463
- Chen, Y.-M., Wild, V., Kauffmann, G., et al. 2009, *MNRAS*, 393, 406
- Chowdhury, A., Kanekar, N., Chengalur, J. N., Sethi, S., & Dwarakanath, K. S. 2020, *Nature*, 586, 369
- Coil, A. L., Newman, J. A., Kaiser, N., et al. 2004, *ApJ*, 617, 765
- Crighton, N. H. M., Murphy, M. T., Prochaska, J. X., et al. 2015, *MNRAS*, 452, 217
- Davis, M., Faber, S. M., Newman, J., et al. 2003, in *Society of Photo-Optical Instrumentation Engineers (SPIE) Conference Series*, ed. P. Guhathakurta, Vol. 4834, 161–172
- Decarli, R., Aravena, M., Boogaard, L., et al. 2020, *ApJ*, 902, 110
- Diemer, B., Stevens, A. R. H., Lagos, C. d. P., et al. 2019, *MNRAS*, 487, 1529
- Eckert, K. D., Kannappan, S. J., Stark, D. V., et al. 2015, *ApJ*, 810, 166
- Faber, S. M., Phillips, A. C., Kibrick, R. I., et al. 2003, in *Society of Photo-Optical Instrumentation Engineers (SPIE) Conference Series*, ed. M. Iye & A. F. M. Moorwood, Vol. 4841, 1657–1669
- Fernández, X., Gim, H. B., van Gorkom, J. H., et al. 2016, *ApJ*, 824, L1
- Fu, J., Guo, Q., Kauffmann, G., & Krumholz, M. R. 2010, *MNRAS*, 409, 515
- Geach, J. E., Smail, I., Moran, S. M., et al. 2011, *ApJ*, 730, L19
- Giovanelli, R., Haynes, M. P., Kent, B. R., et al. 2005, *AJ*, 130, 2598
- Haynes, M. P., Giovanelli, R., Kent, B. R., et al. 2018, *ApJ*, 861, 49
- Jones, M. G., Haynes, M. P., Giovanelli, R., & Moorman, C. 2018, *MNRAS*, 477, 2
- Kanekar, N., Sethi, S., & Dwarakanath, K. S. 2016, *ApJ*, 818, L28
- Kannappan, S. J. 2004, *ApJ*, 611, L89
- Kauffmann, G., Heckman, T. M., White, S. D. M., et al. 2003, *MNRAS*, 341, 33
- Kauffmann, G., Li, C., Zhang, W., & Weinmann, S. 2013, *MNRAS*, 430, 1447
- Kroupa, P. 2001, *MNRAS*, 322, 231
- Lagos, C. D. P., Lacey, C. G., Baugh, C. M., Bower, R. G., & Benson, A. J. 2011, *MNRAS*, 416, 1566
- Lah, P., Chengalur, J. N., Briggs, F. H., et al. 2007, *MNRAS*, 376, 1357
- Lah, P., Pracy, M. B., Chengalur, J. N., et al. 2009, *MNRAS*, 399, 1447
- Li, C., Kauffmann, G., Fu, J., et al. 2012, *MNRAS*, 424, 1471
- Martin, D. C., Fanon, J., Schiminovich, D., et al. 2005, *ApJ*, 619, L1
- Masui, K. W., Switzer, E. R., Banavar, N., et al. 2013, *ApJ*, 763, L20
- Meyer, M. J., Zwaan, M. A., Webster, R. L., et al. 2004, *MNRAS*, 350, 1195
- Neeleman, M., Prochaska, J. X., Ribaudo, J., et al. 2016, *ApJ*, 818, 113
- Newman, J. A., Cooper, M. C., Davis, M., et al. 2013, *ApJS*, 208, 5
- Noeske, K. G., Weiner, B. J., Faber, S. M., et al. 2007, *ApJ*, 660, L43
- Noterdaeme, P., Petitjean, P., Carithers, W. C., et al. 2012, *A&A*, 547, L1
- Obreschkow, D., Klöckner, H. R., Heywood, I., Levrier, F., & Rawlings, S. 2009, *ApJ*, 703, 1890
- Patuarel, G., Theureau, G., Bottinelli, L., et al. 2003, *A&A*, 412, 57
- Pen, U.-L., Staveley-Smith, L., Peterson, J. B., & Chang, T.-C. 2009, *MNRAS*, 394, L6
- Pillepich, A., Springel, V., Nelson, D., et al. 2018, *MNRAS*, 473, 4077
- Popping, G., Somerville, R. S., & Trager, S. C. 2014, *MNRAS*, 442, 2398
- Prochaska, J. X. & Wolfe, A. M. 2009, *ApJ*, 696, 1543
- Rao, S. M., Turnshek, D. A., & Nestor, D. B. 2006, *ApJ*, 636, 610
- Rao, S. M., Turnshek, D. A., Sardane, G. M., & Monier, E. M. 2017, *MNRAS*, 471, 3428
- Salim, S., Charlot, S., Rich, R. M., et al. 2005, *ApJ*, 619, L39
- Sánchez-Ramírez, R., Ellison, S. L., Prochaska, J. X., et al. 2016, *MNRAS*, 456, 4488
- Sanders, D. B. & Mirabel, I. F. 1985, *ApJ*, 298, L31
- Schaye, J., Crain, R. A., Bower, R. G., et al. 2015, *MNRAS*, 446, 521
- Schlegel, D. J., Finkbeiner, D. P., & Davis, M. 1998, *ApJ*, 500, 525
- Stark, D. P. 2016, *ARA&A*, 54, 761
- van Dokkum, P. G. 2008, *ApJ*, 674, 29
- Vogelsberger, M., Genel, S., Springel, V., et al. 2014, *MNRAS*, 444, 1518
- Walter, F., Carilli, C., Neeleman, M., et al. 2020, *ApJ*, 902, 111
- Wang, J., Kauffmann, G., Józsa, G. I. G., et al. 2013, *MNRAS*, 433, 270
- Wang, J., Kauffmann, G., Overzier, R., et al. 2011, *MNRAS*, 412, 1081
- Wang, J., Overzier, R., Kauffmann, G., von der Linden, A., & Kong, X. 2010, *MNRAS*, 401, 433
- Willmer, C. N. A., Faber, S. M., Koo, D. C., et al. 2006, *ApJ*, 647, 853
- Wilson, J. C., Eikenberry, S. S., Henderson, C. P., et al. 2003, in *Society of Photo-Optical Instrumentation Engineers (SPIE) Conference Series*, ed. M. Iye & A. F. M. Moorwood, Vol. 4841, 451–458
- Wyder, T. K., Martin, D. C., Schiminovich, D., et al. 2007, *ApJS*, 173, 293
- Xie, L., De Lucia, G., Hirschmann, M., Fontanot, F., & Zoldan, A. 2017, *MNRAS*, 469, 968
- Young, J. S., Kenney, J., Lord, S. D., & Schloerb, F. P. 1984, *ApJ*, 287, L65
- Zafar, T., Péroux, C., Popping, A., et al. 2013, *A&A*, 556, A141
- Zhang, W., Li, C., Kauffmann, G., & Xiao, T. 2013, *MNRAS*, 429, 2191
- Zhang, W., Li, C., Kauffmann, G., et al. 2009, *MNRAS*, 397, 1243